The atomic electric field distribution in 2D WSe_2

Most properties of solid materials are fundamentally determined by the atomic-scale electric field and charge density distributions. Crystallographic defects can significantly alter this internal field distribution and thus change the material properties. This is particularly striking in the case of 2D materials, which consist of a few or sometimes only a single atomic layer, as e.g. in graphene or silicene. Among the different 2D materials is tungsten diselenide (WSe_2), which is currently intensively studied due to its versatile properties for next generation electronic and optoelectronic applications. In this study, the impact of defects on the electric field and charge density distribution of WSe_2 is revealed using a new, emerging scanning transmission electron microscopy technique, differential phase contrast (DPC) imaging, combined with comparative density functional theory (DFT) simulations. For a missing selenium atomic column, a characteristic electric field distribution in the vicinity of the defect with locally reduced field magnitudes is observed.

2D materials are promising materials for many next-generation applications. Besides graphene, the class of 2D materials comprises many materials such as Mxenes and transition metal dichalcogenides (TMD), which possess a variety of intriguing properties. The optoelectronic properties of TMDs cover a layer number-dependent tunable band gap [1,2] as well as strong spin-orbit [3–5] and light-matter interactions [6,7]. Tungsten diselenide (WSe_2) is such a TMD, which is semiconducting and exhibits either an indirect (bulk) or a direct band gap (monolayer) [2,8]. Thus, WSe_2 is a promising candidate for optoelectronic applications such as single photon emitters [9–13] and ultra-thin field effect transistors [14].

Due to their reduced dimensionality, crystallographic defects and lattice distortions influence the macroscopic properties of 2D materials particularly strong [15]. As point defects are omnipresent for entropic reasons, it is crucial to understand their impact on macroscopic properties for a successful technological integration. One intrinsic property that is strongly influenced by crystallographic defects, but so far has been challenging to investigate experimentally, is the internal electric field distribution of the 2D material.

The aim of this study is to investigate how defects affect the electric field distribtion in 2D WSe_2. This is achieved by using an advanced scanning transmission electron microscopy (STEM) technique, differential phase contrast (DPC) imaging, to measure the electric field of defect free and defective 2D WSe_2. In combination with state-of-the-art lens aberration correction, mapping of the electric field distribution can be achieved with a spatial resolution of approximately 70 pm, which is significantly smaller than the typical distance of atoms in a solid. DPC is thus a promising method to experimentally study the effect of atomic bonds on the local electric field distribution.

Differential phase contrast (DPC)

In STEM-DPC, a convergent electron beam is scanned across the specimen (Fig. 1a). The electric field distribution is measured by evaluating the electron beam intensity distribution after interaction with the specimen at each position of the scan by using a dedicated detector. For this, a

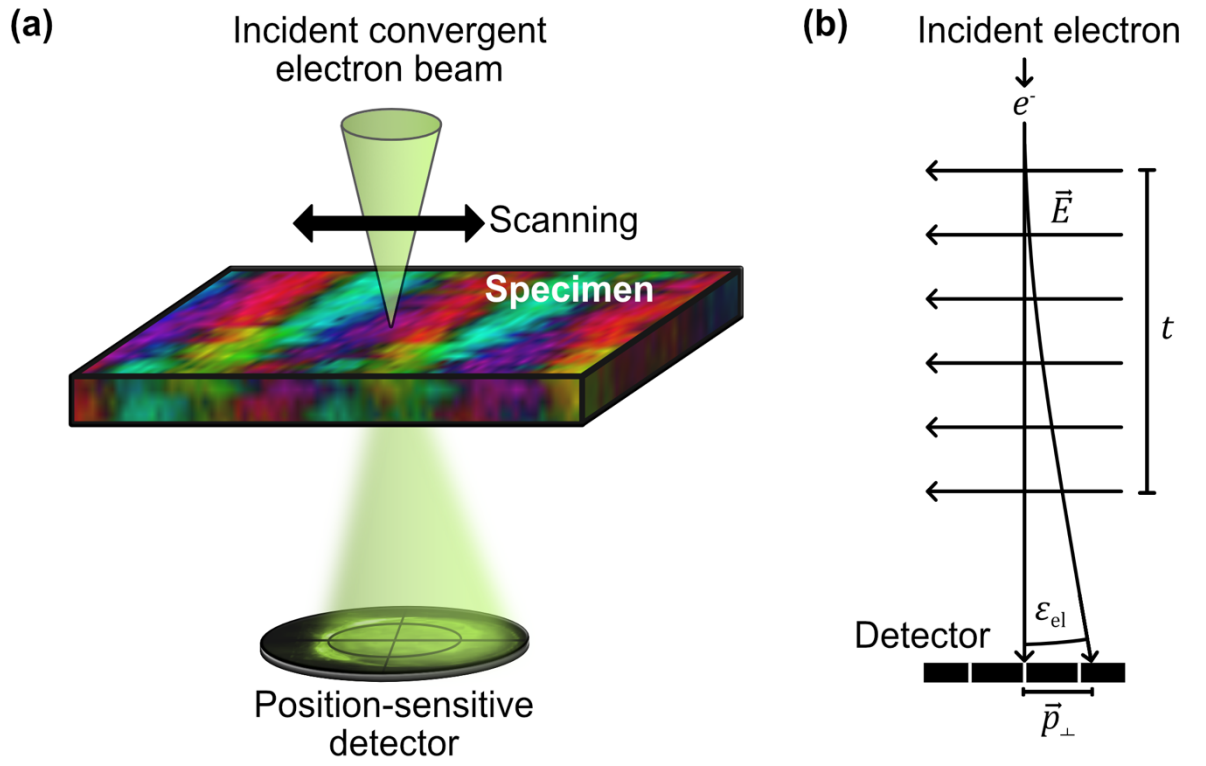

Fig. 1: a) Illustration of differential phase contrast imaging in scanning transmission electron microscopy. b) Electrons in a homogeneous electric field $\vec{E}$ of thickness t experience a lateral momentum transfer $\vec{p}_\perp$ which is related to a deflection angle ε_{el}. Adapted from [16].

position sensitive detector such as a segmented (Fig. 1a) or a pixelated detector can be used.

The contrast mechanism of DPC can be analogized by the interaction of electrons with the homogeneous electric field $\vec{E}$ of a plate capacitor (Fig. 1b). The interaction results in a deflection ($\varepsilon_{\mathrm{el}}$) which is caused by a lateral momentum $\vec{p}_\perp$ transferred to incident electrons by Coulomb forces. For homogeneous electric fields, this lateral momentum is proportional to $\vec{E}_\perp \cdot t$ where $\vec{E}_\perp$ is the electric field perpendicular to the incident electron beam direction and t is the specimen thickness. The lateral momentum transfer leads to a rigid displacement of electron beam intensity on the detector [17].

Atomic electric fields are inhomogeneous in magnitude and direction across the electron beam diameter resulting in a redistribution of intensity (exemplarily illustrated on the detector in Fig. 1a)) and not a rigid shift [18]. It can be shown by quantum mechanical derivations that the center of mass (CoM) of the intensity distribution on the detector is closely related to the projected electric field distribution for sufficiently thin specimens (about 5 nm). To determine the electric field at each position of the scan, it thus suffices to determine the CoM, which in the case of segmented detectors is achieved by calculating the intensity differences of opposing detector segments.

In addition to the electric field distribution $\vec{E}_\perp$, the charge density distribution $\rho_\perp$ can be calculated using Gauss' law $\rho_\perp = \varepsilon_0 \nabla \cdot \vec{E}_\perp$, where ε_0 is the vacuum permittivity and ∇ is the two-dimensional divergence.

Experimental details

The analysis of the electric field distribution of a WSe_2 flake is achieved by comparing experimental and simulated DPC images.

Measurements are conducted using a probe-side spherical aberration corrected JEOL JEM-ARM200F equipped with an eight-fold segmented DPC detector. Simulations are obtained using the multislice algorithm Dr. Probe [19].

TEM specimens with free-standing WSe_2 are obtained by mechanical exfoliation based on the scotch tape technique, followed by a polymere-based transfer to a holey silicon nitride TEM grid. Ultimately, WSe_2 flakes span across the 200 nm-sized holes of the silicon nitride TEM grid, allowing for the analysis of free-standing 2D mono-, bi- or trilayer WSe_2 thin films.

Top-view and side-view schematics of a bilayer WSe_2 crystal structure are shown in Fig. 2a). Due to the stacking sequence of two WSe_2 layers, isolated atomic columns of either pure W (2 W atoms) or pure Se (4 Se atoms) are investigated for an electron beam incident in [0001]-direction. The lattice parameters amount to a=3.29 Å and c=12.9 Å.

Electric fields in pristine WSe_2

Fig. 2b) shows the experimental and simulated high-angle annular dark-field (HAADF) images of a pristine WSe_2 bilayer in [0001]-direction. HAADF imaging is a conventional STEM imaging mode and is typically conducted simulateneously to DPC imaging as it is based on the intensity of electrons scattered to angles far-off the optical axis. The HAADF image contrast is roughly proportional to the atomic number $Z^{\sim 2}$ and thus allows to identify the atomic species as well as the precise position of

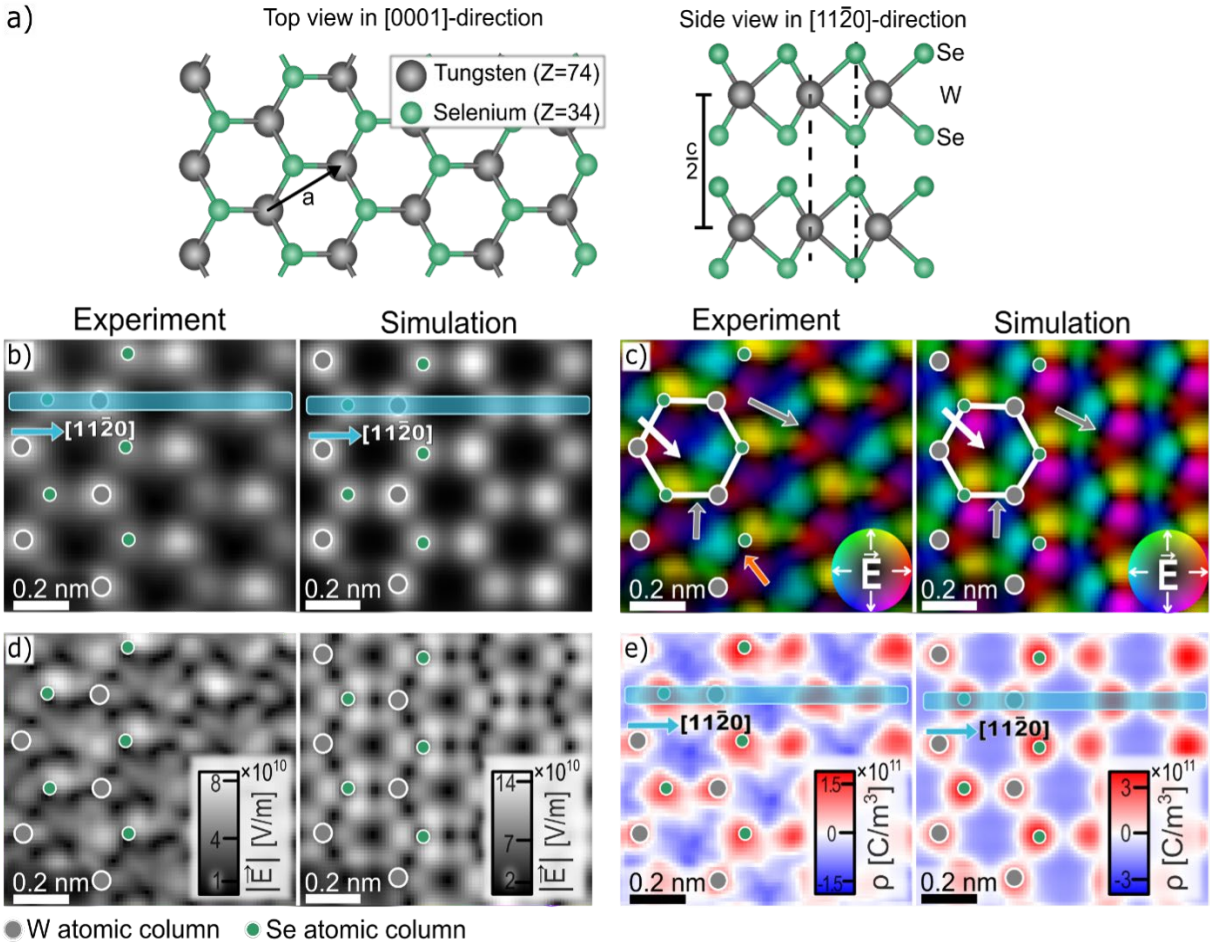

Fig. 2: a) Top- and side-view of a WSe_2 bilayer. b) High-angle annular dark-field image (Line profiles of the blue marked regions are ploted and analysed in the original manuscript). c) Color coded DPC image of the electric field distribution. d) Calculated electric field magnitude and e) charge density. This image is taken from [20].

atomic columns. Results are exemplarily indicated by green and grey dots in Fig. 2b) to e), and are also plotted in all subsequent images.

The experimental and simulated color-coded DPC images revealing the electric field distribution are shown in Fig. 2c). They are visualized by using a color scheme in which the color corresponds to the direction of the electric field and the intensity of the color to the magnitude of the electric field. Both, the measured and simulated electric field distributions are in good agreement, as the electric field distributions exhibit diverging field vectors around the determined atomic columns and no electric field in the vicinity of atomic column centres (red arrow). Reduced transferred momenta resulting from reduced electric field magnitudes are observed between pairs of neighboring atoms where electric fields $\vec{E}$ overlap (grey arrows). Due to the overlap of the opposing electric fields of the six atomic columns in the indicated hexagonal W-Se rings, a local minimum of the projected electric field (marked by white arrows in Fig. 2c)) is observed also near the geometric center of the hexagonal rings. This electric field distribution is in good agreement to that of other hexagonal 2D materials described previously[21,22].

Fig. 2d) depicts the electric field magnitude map calculated from the measurement and the simulation. Measurement and simulation are in good quantitative agreement, i.e. they differ by less than a factor of two. Still, minor structural differences can be observed which include a measured non-zero magnitude at the atomic column position, compared to a zero magnitude in the case of the simulation. In addition, the local minima of projected electric field in the hexagonal ring are not observed in the center of the hexagonal rings. Both findings can be explained by residual lens aberrations and specimen tilt, as is discussed in the original manuscript[20].

The experimental and simulated charge density distributions, which are calculated by applying Gauss' law to the electric field distributions, are displayed in Fig. 2d). Both charge density distributions show localized positive charge density maxima at the atomic column centres surrounded by a delocalized negative charge density. This is expected, as positively charged nuclei are found exactly at the determined atomic column positions and is in good agreement to charge density distributions of other 2D materials reported in literature. Still, the higher positive charge density at the selenium atomic columns compared to those of tungsten should be emphasized. This is not expected, as the projected atomic number of the pure Se atomic column (4x34) is smaller than the one of the pure W atomic column (2x74). However, it can be explained by a dynamic scattering process, which leads to an intensity redistribution from atom to atom within the material. Corrections of the influences of this dynamic scattering process are subject of current research.

Impact of vacancy-type defects

Since 2D materials are prone to defects, studying the impact of defects on the electric field distribution of 2D materials is crucial, as their presence and nature will significantly affect the optoelectrical properties as well as chemical reactivity.

Fig. 3 shows the analysis of a WSe_2 trilayer comprising a vacancy cluster, i.e. a column of six missing Se atoms. The HAADF image

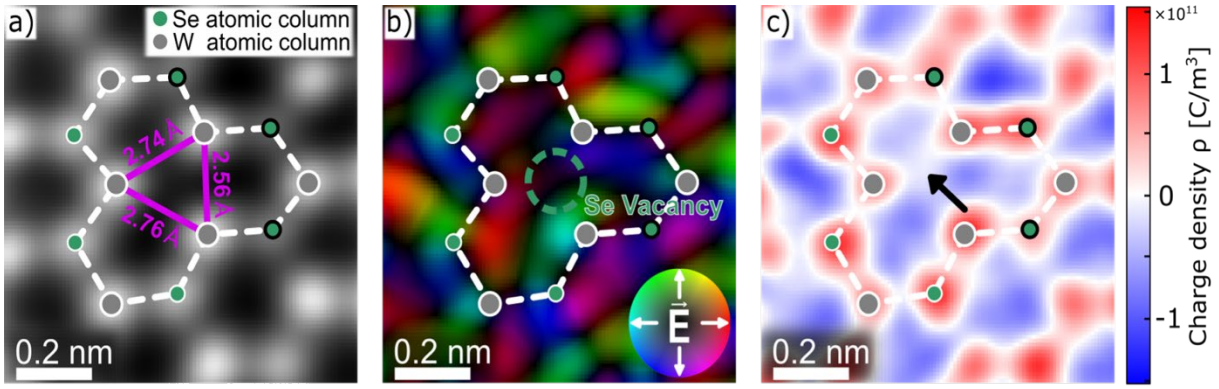

Fig. 3: a) HAADF image of a WSe_2 trilayer with a line-like vacancy cluster. b) Corresponding color coded DPC image of the electric field and c) charge density distributions [20].

in Fig. 3a) gives the precise atomic column positions, while the DPC image in Fig. 3b) displays the electric field distribution and Fig. 3c) the corresponding charge density distribution in the vicinity of the defect.

It is observed that the atomic lattice of the WSe_2 in the vicinity of the defect (dashed lines) is significantly distorted. This is visible in the HAADF image in Fig. 2a) by an inward relaxation of the pure W atomic columns directly adjacent to the defect site (distorted hexagonal rings). The W atoms have an average distance of 2.7 Å. This is smaller than the W-W distance (lattice vector a in Fig. 2a)) in a defect-free WSe_2 monolayer of 3.29 Å. *Ab-initio* DFT simulations, which can predict structural relaxations, give a W-W distance of about 2.76 Å for a completely missing Se atomic column. Since HAADF imaging might be unable to detect light atoms such as oxygen and trapping of O atoms at defect sites in WSe_2 cannot be excluded experimentally, DFT simulations of the impact of substitutional oxygen atoms were conducted revealing a W-W distance of about 2.97 Å if the defect site is decorated by O atoms. Due to this larger W-W distance, a complete O atomic column can be ruled out. Further investigations on substitutional atoms are compiled in the original manuscript[20].

The colour-coded DPC image displayed in Fig. 3 b) again exhibits visible but distorted color wheels around the atomic column positions. In addition, the inverted color wheels within the hexagonal atom rings can be observed in defect free regions. At the position of the defect, no diverging electric field distribution is observable, supporting the interpretation of this defect as a completely missing Se column. This is supported by the charge density map in Fig. 3c) which shows a charge density close to zero at the position of the defect.

To reveal the impact of the defect on the electric field distribution, the defective electric field distribution $\vec{E}_{\mathrm{def}}$ is compared to the electric field $\vec{E}_{\mathrm{pris}}$ of pristine WSe_2 trilayer by calculating the difference $\Delta\vec{E} = \vec{E}_{\mathrm{def}} - \vec{E}_{\mathrm{pris}}$. To compensate for the differences of the atomic column positions of both electric field distributions, a non-rigid registration algorithm is used, which is based on HAADF intensities and aligns the $\vec{E}_{\mathrm{pris}}$ to the $\vec{E}_{\mathrm{def}}$ while accounting for the inward relaxation of W atoms. For the electric field distributions $\vec{E}_{\mathrm{def}}$ and $\vec{E}_{\mathrm{pris}}$, the alignment is conducted in the same way as for the HAADF image.

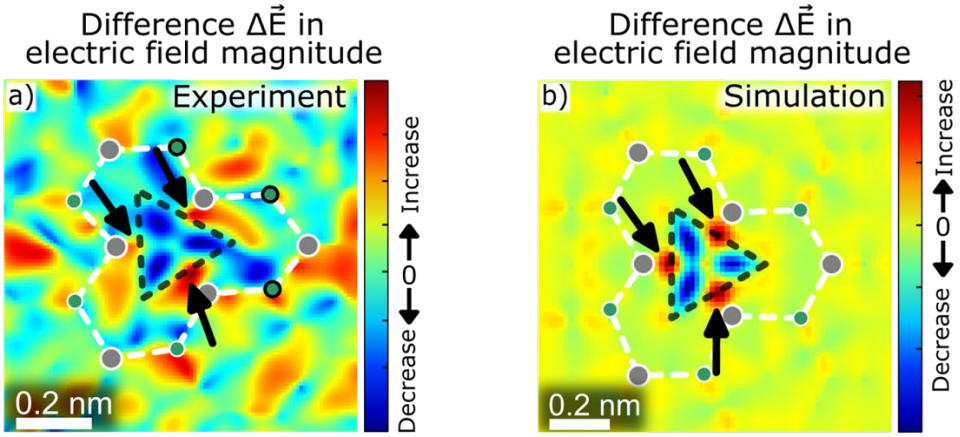

Fig. 4: a) HAADF image of a WSe_2 trilayer with a line-like vacancy cluster. b) Corresponding color coded DPC image of the electric field and c) charge density distributions [20].

The calculated difference map is shown in Fig. 4a), which reveals a triangle shaped region of reduced field magnitude at the defect site. This triangle shaped region comprises a trifoliate feature of more strongly decreased electric field magnitude. Exactly at the defect position, no change in the electric field distribution is observed. This is expected as no electric field magnitude is expected directly at the atom positions as well as for a completely missing atomic column. Furthermore, increased electric field magnitudes are observed at the adjacent W atomic columns (black arrows), which possibly promote adatom trapping. These findings are supported by simulations shown in Fig. 4b) showing similar featues.

Precise insights into the defect-induced characteristic change in the electric field distribution are obtained from DFT simulations of the electron charge density distribution (red) in a defective WSe_2 monolayer (side and top view in Fig. 5). For a completely missing Se_2 atomic column Fig. 5a), the atomic relaxation of the neighbouring W_6Se_6 atoms results in a three-fold crescent-shaped accumulation of electronic charge (around white "x"), pairwise bridging the six adjacent W atoms. This three-fold symmetrical feature qualitatively agrees well to the experimental electric field distributions in Fig. 3 and Fig 4. However, the experimental electric field and charge density distributions do not possess a perfect

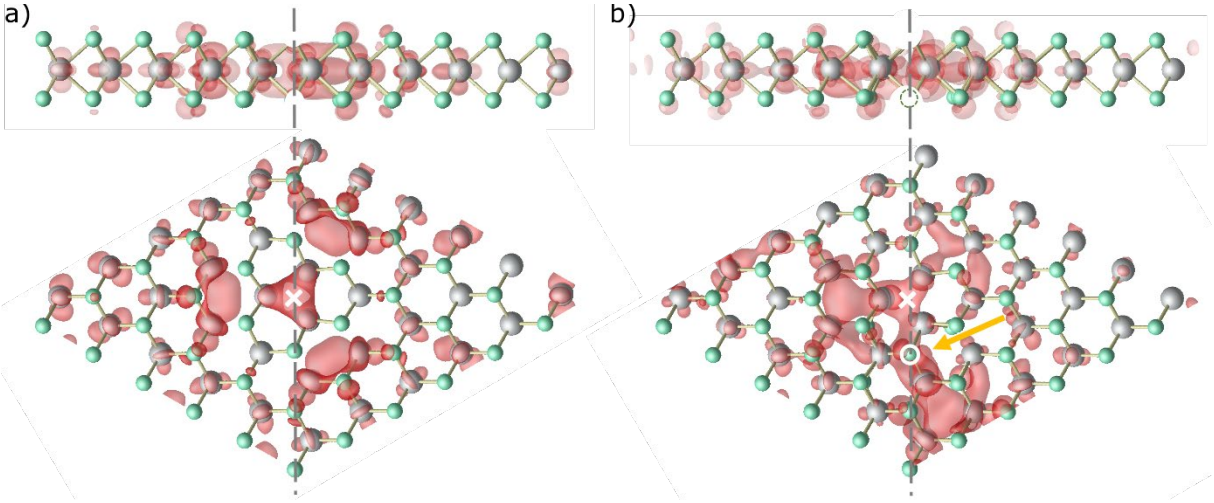

Fig. 5: a) HAADF image of a WSe_2 trilayer with a line-like vacancy cluster. b) Corresponding color coded DPC image of the electric field and c) charge density distributions [20].

three-fold symmetry, which can be explained by further missing Se atoms (not complete atomic columns) in the vicinity of the defect. This is again approved by DFT simulations including another missing Se atom in the vicinity of the defect (2+1 defect) revealing a significant distortion of the defect induced charge density. The absence of further Se atoms was experimentally deduced from the HAADF intensity (compare black and white outlined dots in Fig. 3 and Fig. 4). Further details on the DFT simulations are found in the original manuscript[20].

Conclusions

The interatomic Coulomb fields in pristine and defective WSe_2 flakes are analysed experimentally and theoretically by using one of the emerging scanning transmission electron microscopy techniques, differential phase contrast imaging (DPC). Diverging electric field distributions with electric field vectors pointing away from the nucleic positions are observed around each individual atomic column and quantitatively measured allowing to derive the projected charge density in the 2D material. Positive charge densities are measured at atomic column positions which are surrounded by negative charge densites. Due to a coherent scattering effect, selenium atomic columns exhibit a higher positive charge density compared to tungsten atomic columns. The impact of a Se vacancy-type defect, more precisely a completely missing Se atomic column, on the electric field distribution is studied in addition, revealing a characteristic change. This characteristic change includes an increase of electric field directly at the W atomic columns, which possibly promotes adatom trapping. These findings are supported by multislice STEM image simulations as well as DFT simulations of the defect-induced charge density. All in all, the study presented here shows that STEM-DPC on ultra-thin specimens allows to gain insight into fundamental materials properties at an unprecedented level.

Authors

Maja Groll, Julius Bürger, Ioannis Caltzidis, Klaus D. Jöns, Wolf Gero Schmidt,

Uwe Gerstmann, Jörg K. N. Lindner*

Corresponding author

Prof. Dr. Jörg K. N. Lindner: lindner@physik.upb.de

Methods

Scanning transmission electron microscopy (STEM), differential phase contrast, STEM image simulations, density functional theory simulations, PDMS-based transfer of 2D materials

Original manuscript

Groll, M., et al. "DFT-Assisted Investigation of the Electric Field and Charge Density Distribution of Pristine and Defective 2D WSe_2 by Differential Phase Contrast Imaging." Small (2024): 2311635.

References

[1] J. S. Ponraj, Z.-Q. Xu, S. C. Dhanabalan, H. Mu, Y. Wang, J. Yuan, P. Li, S. Thakur, M. Ashrafi, K. Mccoubrey, Y. Zhang, S. Li, H. Zhang, Q. Bao, *Nanotechnology* **2016**, *27*, 462001.

[2] J. Gusakova, X. Wang, L. L. Shiau, A. Krivosheeva, V. Shaposhnikov, V. Borisenko, V. Gusakov, B. K. Tay, *Phys. Status Solidi A* **2017**, *214*, 1700218.

[3] K. F. Mak, J. Shan, *Nature Photon* **2016**, *10*, 216.

[4] M. Bernardi, C. Ataca, M. Palummo, J. C. Grossman, *Nanophotonics* **2017**, *6*, 479.

[5] D. Xiao, G.-B. Liu, W. Feng, X. Xu, W. Yao, *Phys. Rev. Lett.* **2012**, *108*, 196802.

[6] U. Wurstbauer, B. Miller, E. Parzinger, A. W. Holleitner, *J. Phys. D: Appl. Phys.* **2017**, *50*, 173001.

[7] L. Britnell, R. M. Ribeiro, A. Eckmann, R. Jalil, B. D. Belle, A. Mishchenko, Y.-J. Kim, R. V. Gorbachev, T. Georgiou, S. V. Morozov, A. N. Grigorenko, A. K. Geim, C. Casiraghi, A. H. C. Neto, K. S. Novoselov, *Science* **2013**, *340*, 1311.

[8] T. Tan, X. Jiang, C. Wang, B. Yao, H. Zhang, *Adv. Sci.* **2020**, *7*, 2000058.

[9] P. Tonndorf, R. Schmidt, R. Schneider, J. Kern, M. Buscema, G. A. Steele, A. Castellanos-Gomez, H. S. J. van der Zant, S. M. de Vasconcellos, R. Bratschitsch, *Optica, OPTICA* **2015**, *2*, 347.

[10] A. Srivastava, M. Sidler, A. V. Allain, D. S. Lembke, A. Kis, A. Imamoğlu, *Nature Nanotech* **2015**, *10*, 491.

[11] Y.-M. He, G. Clark, J. R. Schaibley, Y. He, M.-C. Chen, Y.-J. Wei, X. Ding, Q. Zhang, W. Yao, X. Xu, C.-Y. Lu, J.-W. Pan, *Nature Nanotech* **2015**, *10*, 497.

[12] C. Chakraborty, L. Kinnischtzke, K. M. Goodfellow, R. Beams, A. N. Vamivakas, *Nature Nanotech* **2015**, *10*, 507.

[13] C. Errando-Herranz, E. Schöll, R. Picard, M. Laini, S. Gyger, A. W. Elshaari, A. Branny, U. Wennberg, S. Barbat, T. Renaud, M. Sartison, M. Brotons-Gisbert, C. Bonato, B. D. Gerardot, V. Zwiller, K. D. Jöns, *ACS Photonics* **2021**, *8*, 1069.

[14] H. Fang, S. Chuang, T. C. Chang, K. Takei, T. Toshitake, J. Ali, *Nano Letters* **2012**, *12*.

[15] H.-P. Komsa, A. V. Krasheninnikov, in *Defects in Two-Dimensional Materials* (Eds: R. Addou, L. Colombo), Elsevier, **2022**, pp. 7–41.

[16] J. Bürger, (2024) Contributions to differential phase contrast imaging [Doctoral dissertation, Universität Paderborn], https://nbn-resolving.org/urn:nbn:de:hbz:466:2-51885.

[17] K. Müller, F. F. Krause, A. Béché, M. Schowalter, V. Galioit, S. Löffler, J. Verbeeck, J. Zweck, P. Schattschneider, A. Rosenauer, *Nat Commun* **2014**, *5*, 5653.

[18] K. Müller-Caspary, F. F. Krause, T. Grieb, S. Löffler, M. Schowalter, A. Béché, V. Galioit, D. Marquardt, J. Zweck, P. Schattschneider, J. Verbeeck, A. Rosenauer, *Ultramicroscopy* **2017**, *178*, 62.

[19] J. Barthel, *Ultramicroscopy* **2018**, *193*, 1.

[20] M. Groll, J. Bürger, I. Caltzidis, K. D. Jöns, W. G. Schmidt, U. Gerstmann, J. K. N. Lindner, *Small* **2024**, 2311635.

[21] K. Müller-Caspary, M. Duchamp, M. Rösner, V. Migunov, F. Winkler, H. Yang, M. Huth, R. Ritz, M. Simson, S. Ihle, H. Soltau, T. Wehling, R. E. Dunin-Borkowski, S. Van Aert, A. Rosenauer, *Phys. Rev. B* **2018**, *98*, 121408.

[22] N. Shibata, *J. Ceram. Soc. Japan* **2019**, *127*, 708.